Article

Efficient Fizeau drag from Dirac electrons in monolayer graphene

Wenyu Zhao[1,9], Sihan Zhao[1,9], Hongyuan Li[1,2,3], Sheng Wang[1,3], Shaoxin Wang[1], M. Iqbal Bakti Utama[1,3,4], Salman Kahn[1,3], Yue Jiang[1,5], Xiao Xiao[1,5], SeokJae Yoo[1], Kenji Watanabe[6], Takashi Taniguchi[7], Alex Zettl[1,3,8] & Feng Wang[1,3,8 ✉]

Fizeau demonstrated in 1850 that the speed of light can be modified when it is propagating in moving media[1]. However, such control of the light speed has not been achieved efficiently with a fast-moving electron media by passing an electrical current. Because the strong electromagnetic coupling between the electron and light leads to the collective excitation of plasmon polaritons, it is hypothesized that Fizeau drag in electron flow systems manifests as a plasmonic Doppler effect. Experimental observation of the plasmonic Doppler effect in electronic systems has been challenge because the plasmon propagation speed is much faster than the electron drift velocity in conventional noble metals. Here we report direct observation of Fizeau drag of plasmon polaritons in strongly biased monolayer graphene by exploiting the high electron mobility and the slow plasmon propagation of massless Dirac electrons. The large bias current in graphene creates a fast-drifting Dirac electron medium hosting the plasmon polariton. This results in non-reciprocal plasmon propagation, where plasmons moving with the drifting electron media propagate at an enhanced speed. We measure the Doppler-shifted plasmon wavelength using cryogenic near-field infrared nanoscopy, which directly images the plasmon polariton mode in the biased graphene at low temperature. We observe a plasmon wavelength difference of up to 3.6 per cent between a plasmon moving with and a plasmon moving against the drifting electron media. Our findings on the plasmonic Doppler effect provide opportunities for electrical control of non-reciprocal surface plasmon polaritons in non-equilibrium systems.

A surface plasmon polariton—a coupled electromagnetic and electron oscillation mode—has the unique capability to confine and manipulate light at the subwavelength scale[2–5]. The plasmonic enhancement of the light–matter interaction has a key role in nanophotonics[6], ranging from nanoscale nonlinear optics[7] to quantum optics[8] to flat optics[9]. Electrical control of the plasmon polariton is highly desirable in such applications. An intriguing possibility for plasmon control is through Fizeau drag[1], where the moving electron media modulate the propagation speed of the plasmon polariton. This can be viewed as a plasmonic Doppler effect, where counter-propagating plasmons can have different speeds depending on the moving electron media.

The plasmonic Doppler effect is negligibly small in conventional noble metals because the plasmon velocity is more than a million times larger than the highest drift velocity achievable in those metals[3]. Recent theories have predicted that the two-dimensional (2D) Dirac electrons in graphene provide an ideal platform to realize a strong plasmonic Doppler effect due to the combination of low carrier density, high electron mobility and strong plasmon polariton confinement[10–17]. Compared with conventional metals, the electron drift velocity (v_d) in graphene is orders of magnitude higher and can reach a value of 3×10^5 m s^{-1} (ref. [18]). At the same time, the graphene plasmon features an ultrahigh field confinement[14,19–22] ($\lambda_p/\lambda_0 \approx 1/150$, where λ_p is the plasmon wavelength and λ_0 is the excitation light wavelength in free space), resulting in a plasmon group velocity (v_p) of around 2×10^6 m s^{-1}, two orders smaller than the speed of light. A notable plasmonic Doppler effect can emerge in electrically biased graphene when the electron drift velocity v_d reaches a substantial fraction of the plasmon velocity[18,23]. Such a Doppler effect has been predicted to break the time-reversal symmetry in the graphene optical response in the non-local limit and create non-reciprocal surface plasmon propagations[24–31].

Here we report experimental observation of the plasmonic Doppler effect in monolayer graphene. Taking advantage of cryogenic scanning near-field infrared nanoscopy, we can measure the Doppler-induced wavelength shift in real space even under a large bias current in graphene. Our two-terminal graphene device is composed of ultraclean monolayer graphene fully encapsulated in hexagonal boron nitride

[1]Department of Physics, University of California, Berkeley, Berkeley, CA, USA. [2]Graduate Group in Applied Science and Technology, University of California, Berkeley, Berkeley, CA, USA. [3]Materials Science Division, Lawrence Berkeley National Laboratory, Berkeley, CA, USA. [4]Department of Materials Science and Engineering, University of California, Berkeley, Berkeley, CA, USA. [5]Department of Physics, Chinese University of Hong Kong, Hong Kong, China. [6]Research Center for Functional Materials, National Institute for Materials Science, Tsukuba, Japan. [7]International Center for Materials Nanoarchitectonics, National Institute for Materials Science, Tsukuba, Japan. [8]Kavli Energy NanoSciences Institute at University of California Berkeley and Lawrence Berkeley National Laboratory, Berkeley, CA, USA. [9]These authors contributed equally: Wenyu Zhao, Sihan Zhao. ✉e-mail: fengwang76@berkeley.edu
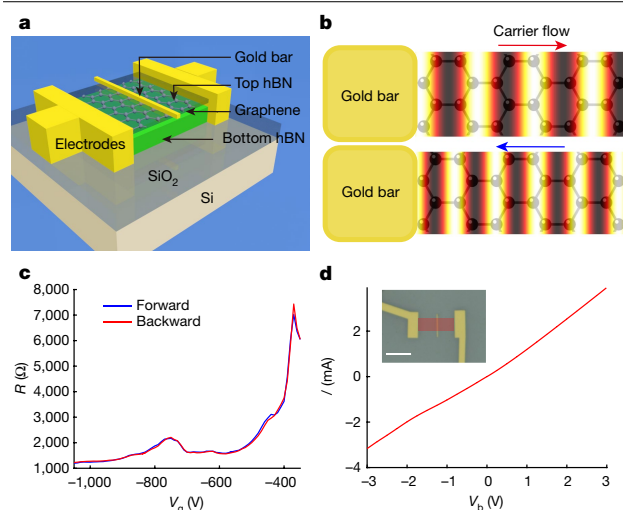
Fig. 1 | Schematic view of the Doppler effect in a graphene device.
a, Schematic of the plasmonic Doppler device, which includes hBN encapsulated graphene, a top gold nanobar as a plasmon launcher and source–drain electrodes with 1D edge contacts for electrically driving the current. **b**, Illustration of the plasmonic Doppler effect in graphene. The sharp edge of the gold nanobar efficiently excites plasmons propagating away from the gold nanobar. The wavelength of propagating plasmons will be shifted due to the drifting electron medium. Plasmons propagating along with the drifting electrons will have an enhanced speed and longer wavelength, whereas plasmons propagating against the drifting electrons will have a shorter wavelength. **c**, Gate-dependent two-terminal resistance R of the graphene device. The resistance decreases quickly with increased carrier doping in the device. The second resistance peak corresponds to the second Dirac point due to unintentional alignment of the graphene and hBN lattice. **d**, I–V curve of the Doppler device at $V_g = -1,050$ V. The two-terminal resistance is about 870 Ω, indicating the high quality of the electrical contact. The inset shows an optical image of the graphene device. Owing to the thick SiO_2 layer, the contrasts of the very thin top hBN and graphene are very weak. The graphene channel is indicated by the red shaded region. Scale bar, 10 μm.

(hBN) and a nanofabricated gold nanobar as the integrated plasmon launcher. The plasmon launched by the gold nanobar is imaged by near-field infrared nanoscopy, and it shows substantial modulation by the electrical bias current (and therefore the electron drift velocity). We quantify the plasmonic Doppler effect by monitoring the plasmon wavelength change for positive and negative electrical current and observe a Doppler-induced wavelength modulation as large as 3.6% for a bias current density of ±0.8 mA μm⁻¹. Our experimental results agree well with the existing theoretical model[30]. This strong plasmonic Doppler effect provides new opportunities for exploring non-equilibrium plasmons[32–35] and non-reciprocal plasmonic[36–38] phenomena in graphene and other high-mobility 2D materials.

Doppler-induced wavelength shift

Figure 1a shows a schematic of our device fabricated on a silicon dioxide/silicon (SiO_2/Si) substrate. Ultraclean monolayer graphene was fully encapsulated by two hBN flakes using the dry-transfer technique (see Methods for details of the sample fabrication). Source–drain electrodes with low contact resistance are fabricated using the 1D edge contact method[39]. The narrow gold nanobar (about 500 nm in width and 9.5 μm in length) in the middle of the device is used to excite the plasmon in the graphene sheet (5 μm in width and 15 μm in length). To access the graphene plasmon efficiently, we use a very thin top hBN layer with a thickness of about 2 nm. Figure 1b shows the Doppler effect of the graphene plasmon launched by the gold nanobar under positive

and negative carrier flow directions. The sharp edge of the gold nanobar serves as an efficient launcher of the plasmon in graphene[12,20], which propagates away from the nanobar. The presence of a carrier flow breaks the time-reversal symmetry ($\omega_{k_x} \neq \omega_{-k_x}$), where ω_{k_x} (ω_{-k_x}) is the plasmon dispersion along (against) the electron drift direction and k_x ($-k_x$) is the wavenumber along (against) the electron drift direction) and results in different plasmonic group velocities depending on the direction of the external driving current[26]. This leads to a stretched (compressed) plasmon wavelength for plasmons propagating along (against) the carrier flow direction. In Fig. 1b, the wavelength change is exaggerated to better illustrate the idea.

We probe the graphene plasmon with a home-built near-field infrared nanoscopy setup at cryogenic temperature (details in Methods). The base temperature of the sample is fixed at 25 K, which helps to dissipate the unintended Joule heating caused by the large current through the graphene channel. In addition, the phonon scattering of the graphene plasmon is strongly suppressed at low temperature, resulting in a higher plasmon quality factor[3,12] and thus a better accuracy in determining the plasmon wavelength. To probe the graphene plasmon, a 10.6-μm carbon dioxide laser was focused on the sample by an aspheric zinc selenide lens with a spot size of around 10 μm. This guarantees a uniform light illumination on the nanobar and atomic force microscope (AFM) tip when scanning around the bar area (within a range of 1 μm), with negligibly small intensity and phase inhomogeneity. Basically, the graphene nanobar plasmon excited by the gold nanobar propagates away from the bar edge. The propagating plasmon is later scattered by the tip apex, interferes with the background scattered light and gets detected by a mercury cadmium telluride detector in the far field. By scanning along the plasmon propagation direction and recording the near-field interference fringes, we can determine the plasmon wavelength accurately[12,19–21,40]. Figure 1c shows the gate-dependent resistance of a representative Doppler device at 25 K. This specific device has 2-μm-thick SiO_2 dielectrics to minimize the doping change induced by the bias voltage (V_b) required in the Doppler measurements. Only the hole doping data are measured because such a device with thick SiO_2 dielectrics breaks down easily under a high positive backgate voltage V_g (Methods). The device resistance decreases quickly with increased doping away from the charge neutral point at $V_g = -380$ V. The small resistance peak at $V_g = -780$ V is presumably due the graphene/boron nitride moiré superlattice. There is little hysteresis between the forward (blue trace) and backward (red trace) gate voltage scan. Figure 1d shows the channel current of the same device as a function of V_b at $V_g = -1,050$ V, corresponding to a carrier density of $|n| = 7.2 \times 10^{12}$ cm⁻² based on the capacitance model (Methods). Doppler measurements are carried out at this doping, where high-quality plasmons at mid-infrared wavelengths are present. The two-terminal resistance at high doping is dominated by the electrical contact. Using the 1D edge contact, we achieve a low contact resistance of around 870 Ω (slope of the linear fit of Fig. 1d), which allows us to drive large electrical current through the graphene device.

Figure 2 shows the near-field signal under different driving currents. The data are collected from scanning the same line along the plasmon propagating direction, which is perpendicular to the nanobar. At different currents, the graphene plasmons behave quite differently, not only because of the Doppler-induced wavelength shift but also because of a temperature change due to the strong Joule heating. The temperature change has two effects. First, plasmon damping increases with temperature, which leads to a decreased near-field signal in amplitude; second, thermal expansion and other effects can modify the background light scattering and thus modulate the near-field interference signal. To eliminate these complexities induced by the thermal effects, we directly compare the plasmon wavelengths for positive and negative currents of the same magnitude, which have the same thermal load in the device but generate the opposite Doppler shift. Figure 2a shows the 2D near-field signal images obtained from stacking 30 consecutive
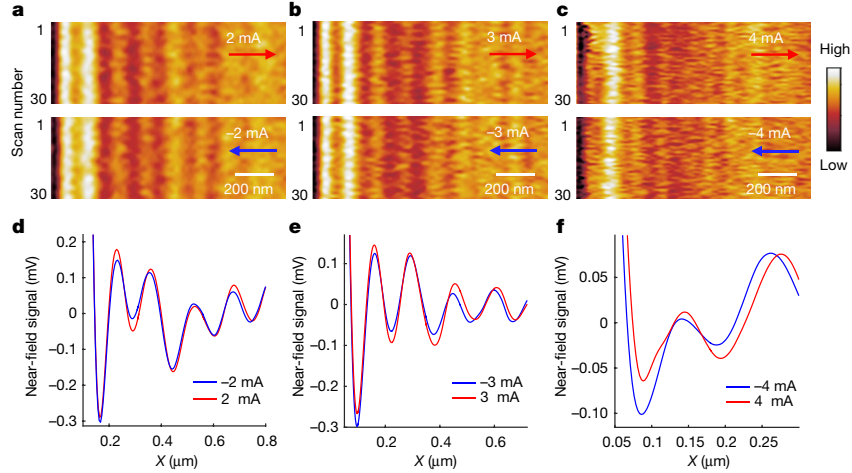
Fig. 2 | Near-field signal of the propagating plasmons under different driving currents. a–c, Near-field data at +2 mA and −2 mA (**a**), +3 mA and −3 mA (**b**) and (**c**) +4 mA and −4 mA. Data from 30 consecutive scans along the same line on the sample are shown. The gold nanobar is located on the left and the graphene plasmons are launched and propagate to the right. The red and blue arrows indicate the carrier flow directions. **d–f**, The corresponding line profiles averaged over the 30 scans shown in **a–c**, respectively. During the measurement, the AFM is controlled to always scan the same line on the sample while recording the third-order harmonics of the near-field signal. The amplitude of the near-field signal degrades at large current, presumably due to Joule heating in the device. The Doppler effect induces a wavelength increase of 1.2%, 2.2% and 3.6% for 2 mA, 3 mA and 4 mA relative to their negative current counterpart, respectively. The wavelength shift is estimated by averaging the wavelength shifts for consecutive interference extrema positions in the near-field line profiles shown in **d–f**.

scans of a single line at +2 mA and −2 mA. Figure 2d shows the line profile obtained by averaging 30 scans to improve the signal-to-noise ratio. The wavelength at +2 mA is stretched by 1.2% compared with at −2 mA, which is determined by averaging the wavelength shifts at the interference peaks and dips in the line profile in Fig. 2d. Figure 2b, e shows the measured near-field signals when the current increases to about ±3 mA. The difference between the shift induced by the positive current and the shift induced by the negative current becomes more prominent. We observe a total Doppler-induced wavelength shift of about 2.2% between +3 mA and −3 mA. The largest wavelength shift we can observe reaches about 3.6% between +4 mA and −4 mA (Fig. 2c, f). At currents higher than ±4 mA, the plasmons become very weak and are beyond the detection limit of our setup, presumably due to the substantial thermal heating. A similar Doppler shift has been observed in other graphene devices (Methods). In principle, the Doppler-induced wavelength shift can be larger at low carrier density, because a larger carrier drift velocity can be realized at low doping with the same thermal load. Experimentally, however, the graphene plasmon becomes quite weak at low carrier doping and accurate measurements of the plasmons are very challenging with 10.6-µm laser excitation.
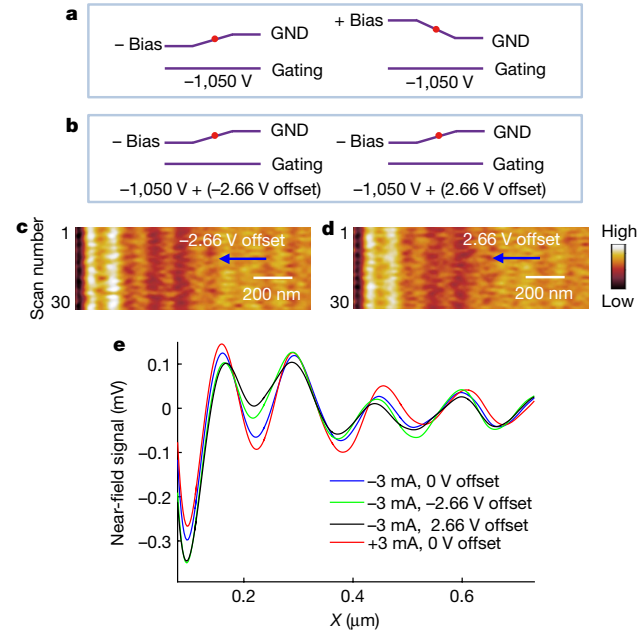
Non-uniform doping effects

Next we rule out the possibility of a doping-induced wavelength shift in our experimental observation. To achieve large carrier drift velocity, the applied bias (V_b) is on the order of few volts. The switching of the current direction by switching the sign of V_b will result in some changes in the local graphene doping level, which in turn gives rise to a finite wavelength shift. Figure 3a illustrates the V_b-induced doping change in the graphene channel with positive and negative V_b. In some devices, we used an SiO₂/Si substrate with a 2-µm-thick oxide layer to substantially reduce this side effect. We experimentally investigate the graphene near-field response with changing V_g (as schematically shown in Fig. 3b). The graphene channel is fixed at −3 mA whereas V_g is varied by adding an offset of ±2.66 V (the bias voltage to achieve a current of about ±3 mA) to −1,050 V. Figure 3c, d shows the near-field infrared nanoscopy data for the graphene plasmons with an offset backgate

voltage of −2.66 V and +2.66 V, respectively. Figure 3e shows the line profiles of the near-field signal with a bias current of −3 mA and an offset voltage of 0 V (blue trace), −2.66 V (green trace) and 2.66 V (black trace), which are compared with the near-field signal with a bias current of +3 mA and an offset voltage of 0 V (red trace). The wavelength shift between ±2.66 V offset gate conditions at −3 mA (green and black traces) is 0.34%, and this gives a gate-induced wavelength shift of 0.06% per volt, which is consistent with the theoretical predicted value of 0.07% per volt for our device conditions[20]. In the middle of the graphene channel where we performed the measurements, the gate voltage change due to the reversal of the current directions between ±3 mA is around 2.66 V, and this corresponds to a gate-induced wavelength shift of 0.17%. Therefore, the doping-induced wavelength change is over an order of magnitude smaller than the measured Doppler induced shift (around 2.2% in Fig. 2b, e). We note that the doping effect for Si/SiO₂ devices with 285-nm SiO₂ will be stronger, but the Doppler wavelength shift will still be much larger than the doping-induced wavelength change.

Non-equilibrium plasmon response

The non-equilibrium plasmon response of the current-carrying monolayer graphene can be calculated using the linear response theory[30]. The density–density response function of current-carrying states can be analytically approximated by employing the random phase approximation[30]. The analytical form of graphene plasmon dispersion ($\omega_{pl}(k)$) under a biased condition can then be expressed as $\omega_{pl}(k) = \sqrt{\frac{2D_0 W(\beta)}{\varepsilon\beta}} \sqrt{k}\left[1 + \gamma\frac{\sqrt{2\beta W(\beta)}}{4}\sqrt{\frac{k}{k_{TF}}} + \frac{12 - 16\alpha_{ee}{}^2 - 3\beta W(\beta)}{16}\frac{k}{k_{TF}}\right]$, $W(\beta) = 2\frac{1 - \sqrt{1 - \beta^2}}{\beta}$ and $\alpha_{ee} = \frac{e^2}{\varepsilon\hbar v_F}$. Here $\gamma = \pm 1$ denotes plasmon propagation along and against the carrier flow direction and $\beta = v_d/v_F$ is the normalized electron drift velocity relative to the Fermi velocity $v_F = 0.85 \times 10^6$ m s⁻¹. $D_0 = \frac{e^2 E_F}{\hbar^2}$ is the Drude weight of non-interacting 2D massless Dirac fermions expressed in terms of the electron charge e, Fermi energy E_F and the reduced Planck constant $\hbar$. $k_{TF} = 4\alpha_{ee}k_F$ is the Thomas–Fermi screening wavevector at temperature $T = 0$ K (ref. [41]), and ε and k_F are the effective dielectric constant of hBN and the Fermi

Article

Fig. 3 | Gating dependence of graphene plasmon wavelength. a, Illustration of the non-uniform doping of the Doppler device at a bias current of ±3 mA under a fixed $V_g = -1,050$ V. The corresponding bias voltage is 2.66 V. The middle area of the graphene experiences different effective gating voltages for positive bias and negative bias. A negative V_b results in a decreased hole doping whereas a positive V_b leads to an increased hole doping. The red dot indicates the electrical potential in the middle of the graphene where we performed the near-field measurements. GND, electrical ground. **b**, Illustration of the control measurements to determine the gating-induced plasmon wavelength change under a driving current. The electrical current in graphene is kept at −3 V, while the backgate voltage is varied by ±2.66 V. **c**, **d**, The near-field infrared nanoscopy data of the graphene plasmons with an offset backgate voltage of −2.66 V (**c**) and +2.66 V (**d**). The blue arrows indicate the carrier flow directions. **e**, Line profiles of the near-field signal with a bias current of −3 mA and an offset voltage of 0 V (blue trace), −2.66 V (green trace) and 2.66 V (black trace), which are compared with the near-field signal with a bias current of +3 mA and an offset voltage of 0 V (red trace). It shows that the doping-induced wavelength change is negligible compared with the experimentally observed Doppler-induced shift in the device.

wavevector. The drift electrons break the time-reversal symmetry and make the graphene plasmon propagation non-reciprocal (Fig. 4a). In the absence of the drift current (that is, $v_d = 0$), the $\omega \approx k$ dispersion curve is formed by two symmetric branches (blue curves in Fig. 4a) corresponding to two counter-propagating waves. The two branches are linked by $\omega_{k_x} = \omega_{-k_x}$, in agreement with the reciprocity and parity symmetries of the system. In contrast, with the drift current flow (Fig. 4b), there is an evident symmetry breaking of the surface plasmon polariton dispersion such that the positive and negative directions become non-degenerate. The forward current (upstream) lifts the dispersion and the backward current (downstream) depresses the dispersion, resulting in a wavelength shift in the plasmon. The asymmetry of the dispersion curve becomes more prominent when the drift velocity increases. Figure 4c shows our experimental data for the plasmon wavevector shift between positive and negative electrical current (symbols) at different ratios of drift velocity over plasmon velocity (v_d/v_p). The green line in Fig. 4c shows the theoretical prediction, which is obtained by calculating the difference between the upstream and downstream dispersion curves in Fig. 4b. The experimental values of v_d are obtained using the equation $v_d = J/ne = I/new$, where J is the current density, I is the driving current, $w = 5$ μm is the width of the graphene device and the carrier density $|n| = 7.2 \times 10^{12}$ cm^{-2}. The plasmon velocity v_p is directly obtained from the measured plasmon wavelength λ_p with the relation $v_p = \lambda_p \times f$, where $f = 28.3$ THz is the probing laser frequency. At a driving current of ±3 mA, switching of the current direction yields a total carrier drift velocity change of around 1.04×10^5 m s^{-1}, corresponding to about 2.4% of the plasmon velocity. The observed Doppler-induced shift reaches about 2.2%. Our experimental observations are consistent with the theoretical predictions, as shown in Fig. 4c.

To achieve stronger Doppler shift and non-reciprocal propagation, we need to further increase the carrier drift velocities[24,26–30] with higher bias current. This can potentially be achieved by implementing a more effective heat sink and by using double-layer graphene[42]. Another approach is to use short electrical driving pulses, which have much lower duty cycle and can avoid undesirable Joule heating effects. These future improvements can substantially increase the achievable carrier drift velocity and enhance the Fizeau drag effects in graphene, which will provide new opportunities to study unidirectional plasmonic phenomena and highly non-equilibrium plasmons.

Note added in proof: After the completion of this work, we became aware of the results of Y. Dong et al.[45].
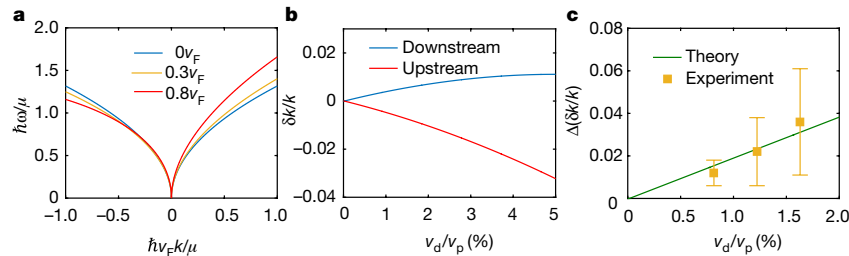
Fig. 4 | Graphene plasmon dispersion and Doppler-induced wavelength shift. a, Plasmon dispersion calculated from the linear response function theory under different carrier drift velocities[30]. The drift carrier velocity dramatically modifies the dispersion of the plasmon and results in non-reciprocal plasmon propagation. For $v_d > 0$ ($v_d < 0$), the carriers propagate parallel (antiparallel) to the plasmons. Plasmons propagating with the drift are blueshifted for a given wavevector and have a higher group velocity. Conversely, the plasmons propagating antiparallel to the drift velocity are redshifted and have a lower group velocity. These effects increase with higher electron drift velocity. **b**, Wavelength shift of the graphene plasmon under different carrier drift velocities for the downstream and upstream branches ($v_F = 0.85 \times 10^6$ m s^{-1}, $\varepsilon = 5.45$)[43,44]. The plasmon energy is set the same as the laser probing energy (around 117 meV). The two branches show very different behaviour at high drift velocities. **c**, Experimental data for the plasmon wavevector shift between the positive and negative bias current (symbols) and the corresponding theoretical prediction (green line) at different electron drift velocities. The experimental error bar is determined from the statistics of the wavelength shift calculated at different extrema of the near-field signal in Fig. 2.

Online content

Any methods, additional references, Nature Research reporting summaries, source data, extended data, supplementary information, acknowledgements, peer review information; details of author contributions and competing interests; and statements of data and code availability are available at https://doi.org/10.1038/s41586-021-03574-4.

1. Foucault, L. Méthode générale pour mesurer la vitesse de la lumière dans l'air et les milieux transparents. Vitesses relatives de la lumière dans l'air et dans l'eau. Projet d'expérience sur la vitesse de propagation du calorique rayonnant. *C. R. Acad. Sci.* **30**, 551–560 (1850).
2. Christensen, T. in *From Classical to Quantum Plasmonics in Three and Two Dimensions* 13–35 (Springer, 2017).
3. Maier, S. A. *Plasmonics: Fundamentals and Applications* (Springer Science & Business Media, 2007).
4. Jablan, M., Soljačić, M. & Buljan, H. Plasmons in graphene: fundamental properties and potential applications. *Proc. IEEE* **101**, 1689–1704 (2013).
5. Low, T. et al. Polaritons in layered two-dimensional materials. *Nat. Mater.* **16**, 182–194 (2017).
6. Novotny, L. & Hecht, B. *Principles of Nano-optics* (Cambridge Univ. Press, 2012).
7. Kauranen, M. & Zayats, A. V. Nonlinear plasmonics. *Nat. Photon.* **6**, 737–748 (2012).
8. Bozhevolnyi, S. I., Martin-Moreno, L. & Garcia-Vidal, F. *Quantum Plasmonics* (Springer, 2017).
9. Yu, N. & Capasso, F. Flat optics with designer metasurfaces. *Nat. Mater.* **13**, 139–150 (2014).
10. Xia, F., Wang, H., Xiao, D., Dubey, M. & Ramasubramaniam, A. Two-dimensional material nanophotonics. *Nat. Photon.* **8**, 899–907 (2014).
11. Castro Neto, A. H., Guinea, F., Peres, N. M., Novoselov, K. S. & Geim, A. K. The electronic properties of graphene. *Rev. Mod. Phys.* **81**, 109–162 (2009).
12. Ni, G. et al. Fundamental limits to graphene plasmonics. *Nature* **557**, 530–533 (2018).
13. Koppens, F. H., Chang, D. E. & Garcia de Abajo, F. J. Graphene plasmonics: a platform for strong light–matter interactions. *Nano Lett.* **11**, 3370–3377 (2011).
14. Dean, C. R. et al. Boron nitride substrates for high-quality graphene electronics. *Nat. Nanotechnol.* **5**, 722–726 (2010).
15. Mak, K. F. et al. Measurement of the optical conductivity of graphene. *Phys. Rev. Lett.* **101**, 196405 (2008).
16. Zhang, Y., Small, J. P., Pontius, W. V. & Kim, P. Fabrication and electric-field-dependent transport measurements of mesoscopic graphite devices. *Appl. Phys. Lett.* **86**, 073104 (2005).
17. Yu, Y.-J. et al. Tuning the graphene work function by electric field effect. *Nano Lett.* **9**, 3430–3434 (2009).
18. Dorgan, V. E., Bae, M.-H. & Pop, E. Mobility and saturation velocity in graphene on SiO_2. *Appl. Phys. Lett.* **97**, 082112 (2010).
19. Woessner, A. et al. Highly confined low-loss plasmons in graphene–boron nitride heterostructures. *Nat. Mater.* **14**, 421–425 (2015).
20. Fei, Z. et al. Gate-tuning of graphene plasmons revealed by infrared nano-imaging. *Nature* **487**, 82–85 (2012).
21. Chen, J. et al. Optical nano-imaging of gate-tunable graphene plasmons. *Nature* **487**, 77–81 (2012).
22. Jablan, M., Buljan, H. & Soljačić, M. Plasmonics in graphene at infrared frequencies. *Phys. Rev. B* **80**, 245435 (2009).
23. Ramamoorthy, H. et al. "Freeing" graphene from its substrate: observing intrinsic velocity saturation with rapid electrical pulsing. *Nano Lett.* **16**, 399–403 (2016).
24. Borgnia, D. S., Phan, T. V. & Levitov, L. S. Quasi-relativistic Doppler effect and non-reciprocal plasmons in graphene. Preprint at https://arxiv.org/abs/1512.09044 (2015).
25. Correas-Serrano, D. & Gomez-Diaz, J. Non-reciprocal and collimated surface plasmons in drift-biased graphene metasurfaces. *Phys. Rev. B* **100**, 081410 (2019).
26. Morgado, T. A. & Silveirinha, M. G. Drift-induced unidirectional graphene plasmons. *ACS Photon.* **5**, 4253–4258 (2018).
27. Sabbaghi, M., Lee, H.-W. & Stauber, T. Electro-optics of current-carrying graphene. *Phys. Rev. B* **98**, 075424 (2018).
28. Sabbaghi, M., Lee, H.-W., Stauber, T. & Kim, K. S. Drift-induced modifications to the dynamical polarization of graphene. *Phys. Rev. B* **92**, 195429 (2015).
29. Wenger, T., Viola, G., Kinaret, J., Fogelström, M. & Tassin, P. Current-controlled light scattering and asymmetric plasmon propagation in graphene. *Phys. Rev. B* **97**, 085419 (2018).
30. Van Duppen, B., Tomadin, A., Grigorenko, A. N. & Polini, M. Current-induced birefringent absorption and non-reciprocal plasmons in graphene. *2D Mater.* **3**, 015011 (2016).
31. Song, J. C. & Rudner, M. S. Chiral plasmons without magnetic field. *Proc. Natl Acad. Sci. USA* **113**, 4658–4663 (2016).
32. Hamm, J. M., Page, A. F., Bravo-Abad, J., Garcia-Vidal, F. J. & Hess, O. Nonequilibrium plasmon emission drives ultrafast carrier relaxation dynamics in photoexcited graphene. *Phys. Rev. B* **93**, 041408 (2016).
33. Morgado, T. A. & Silveirinha, M. G. Negative Landau damping in bilayer graphene. *Phys. Rev. Lett.* **119**, 133901 (2017).
34. Ni, G. et al. Ultrafast optical switching of infrared plasmon polaritons in high-mobility graphene. *Nat. Photon.* **10**, 244–247 (2016).
35. Page, A. F., Ballout, F., Hess, O. & Hamm, J. M. Nonequilibrium plasmons with gain in graphene. *Phys. Rev. B* **91**, 075404 (2015).
36. Lin, X. et al. Unidirectional surface plasmons in nonreciprocal graphene. *New J. Phys.* **15**, 113003 (2013).
37. Wang, Z., Chong, Y., Joannopoulos, J. D. & Soljačić, M. Reflection-free one-way edge modes in a gyromagnetic photonic crystal. *Phys. Rev. Lett.* **100**, 013905 (2008).
38. Yu, Z., Veronis, G., Wang, Z. & Fan, S. One-way electromagnetic waveguide formed at the interface between a plasmonic metal under a static magnetic field and a photonic crystal. *Phys. Rev. Lett.* **100**, 023902 (2008).
39. Wang, L. et al. One-dimensional electrical contact to a two-dimensional material. *Science* **342**, 614–617 (2013).
40. Ocelic, N., Huber, A. & Hillenbrand, R. Pseudoheterodyne detection for background-free near-field spectroscopy. *Appl. Phys. Lett.* **89**, 101124 (2006).
41. Kotov, V. N., Uchoa, B., Pereira, V. M., Guinea, F. & Neto, A. C. Electron–electron interactions in graphene: current status and perspectives. *Rev. Mod. Phys.* **84**, 1067–1125 (2012).
42. Morgado, T. A. & Silveirinha, M. G. Nonlocal effects and enhanced nonreciprocity in current-driven graphene systems. *Phys. Rev. B* **102**, 075102 (2020).
43. Geick, R., Perry, C. & Rupprecht, G. Normal modes in hexagonal boron nitride. *Phys. Rev.* **146**, 543–547 (1966).
44. Hwang, C. et al. Fermi velocity engineering in graphene by substrate modification. *Sci. Rep.* **2**, 590 (2012).
45. Dong, Y. et al. Fizeau drag in graphene plasmonics. *Nature* https://www.nature.com/articles/s41586-021-03640-x (2021).

Article

Methods

Encapsulated graphene device for near-field infrared nanoscopy measurements

We used a dry transfer method with a propylene carbonate (PPC) stamp to fabricate the hBN-encapsulated graphene sample. Thin hBN (2 nm), monolayer graphene and a thick layer of hBN were first exfoliated onto Si substrates with a 285-nm SiO_2 layer. We then used a PPC stamp to pick up the thick layer of hBN, graphene and the thin hBN in sequence to fully encapsulate the graphene channel. To obtain an ultraclean surface, the PPC stamp with the above heterostructure was then flipped over and stamped onto a clean SiO_2/Si substrate with either 2-μm or 285-nm SiO_2 dielectrics thickness. Encapsulated graphene samples were made into devices with 1D edge contacts. In brief, standard e-beam lithography was used to open graphene contact windows on the Polymethyl methacrylate (PMMA)-coated (PMMA 950 A4) sample substrates. Reactive ion etching with CHF_3 and O_2 etching gases (40 s.c.c.m. and 6 s.c.c.m.) was used to etch hBN to expose graphene edges with saw-tooth edge shapes. A separate e-beam lithography process was then carried out to design the electrode patterns of a two-terminal device and a narrow nanobar structure in the middle of graphene. Immediately before the metal deposition, the samples were treated with mild oxygen plasma to expose a clean graphene edges. A chromium/gold (typically 5 nm/75 nm) electrode was made using an e-beam evaporator equipped with a water-cooling system at high vacuum (<1 × 10^{-6} torr). The surfaces of the devices were cleaned by a mild hydrogen plasma treatment (250 °C, 10 s.c.c.m. H_2) for about 30 min. The treated devices were kept in a conductive case for one or two days to avoid potential charging issues before any near-field infrared nanoscopy measurements.

Cryogenic near-field infrared nanoscopy measurements

Our cryogenic near-field infrared nanoscope was based on a home-made AFM that has the capability to work at high vacuum and low temperature. The whole AFM setup was built inside a closed-cycle cryostat, and the AFM head was connected to the cold plate by a soft copper braid to dampen the vibration from the pulse tube. The lowest sample temperature achieved in our AFM system was 25 K. A carbon dioxide laser was coupled into the vacuum chamber through an aspheric zinc selenide lens with 0.45 numerical aperture. The position of the lens was controlled by a vacuum compatible stage. The backscattered light from the tip was collected by a mercury cadmium telluride detector in a self-homodyne configuration and the near-field signal was demodulated at the third harmonic of the tapping frequency to suppress the background. To increase the signal-to-noise ratio, the time constant was set to 10 mS. During the scanning, the turbo pump was turned off to minimize the mechanical vibration. The background vacuum level remained below 1 × 10^{-6} mbar through all the measurements.

Estimation of carrier density in graphene

The dielectrics in the plate capacitator formed between the graphene and the Si backgate were composed of the SiO_2 dielectrics (medium 1) and the bottom hBN layer (medium 2). The total geometric capacitance per unit area was calculated from the expression $\frac{1}{C_{total}} = \frac{1}{C_1} + \frac{1}{C_2}$, where $C_1 = \epsilon_0 \varepsilon_{r1}/d_1$ and $C_2 = \epsilon_0 \varepsilon_{r2}/d_2$ are the capacitance per unit area of SiO_2 and hBN, ϵ_0 is the vacuum permittivity, $\varepsilon_{r1} = \varepsilon_{r2} = 3.9$. For the device measured in Figs. 2, 3, $d_1 = 2$ μm and $d_2 = 40$ nm. The carrier density was obtained by $n = C_{total} \times V_g$, where V_g was measured relative to the charge neutrality point.

In situ electrical gating and transport measurement of the device

The very high backgate voltage used for the device on 2-μm-thick SiO_2 dielectrics could trigger gas ionization in the vacuum. To protect the sample from sudden discharging breakdown, we scanned the backgate voltage slowly (0.5 V s^{-1}) at the hole doping side for several rounds to make sure that the response of the device becomes stable (Keithley 2410). During the scanning of the backgate voltage, the conductance of the device was monitored with a d.c. bias of 1 mV (Keithley 2614B). Electron drift velocity at a fixed backgate voltage was controlled by varying the amplitude and polarity of the d.c. bias (Keithley 2614B).

Doppler-induced wavelength shift in a second device

Extended Data Figs. 1–4 show the plasmonic Doppler effect in another device with 285-nm-thick SiO_2 dielectrics. The width of the graphene channel is $w = 2.5$ μm, and the near-field measurements are performed at a carrier density of 7.0×10^{12} cm^{-2}. In this device, we are able to measure high-quality plasmons propagating on both sides of the gold nanobar. The graphene channel current at discrete bias voltages measured at the same doping condition and temperature is shown in Extended Data Fig. 1. In the high bias condition, the resistance of the two-terminal device is about 1.5 kΩ, indicating a low contact resistance for this narrow channel device.

On the left side of the gold nanobar, the negative current flow enhances the plasmon speed and results in a stretched plasmon wavelength, whereas the positive current flow reduces the plasmon speed with a compressed plasmon wavelength. Extended Data Fig. 2c shows the 2D images of near-field signals at ±0.4 mA where 30 consecutive scans along the same line are recorded. The gold nanobar is located on the right. The graphene plasmons are launched and propagate to the left, which is consistent with the schematics in Extended Data Fig. 2a, b. A current of ±0.4 mA generates a minor shift of plasmon wavelength (around 1.1%) as shown in the line profile in Extended Data Fig. 2d (average from 30 line scans in Extended Data Fig. 2c). As we increase the current to ±1.2 mA, the plasmon wavelength difference becomes more prominent (around 2.3% in Extended Data Fig. 2f). When the current reaches +1.7 mA and −1.9 mA, the wavelength shift becomes about 3.1%. The wavelength shift is extracted by averaging the shift at the interference extrema.

On the right side of the gold nanobar (Extended Data Fig. 3), the plasmon wavelength shift due to the Doppler effect is reversed. The negative current flow will generate a compressed wavelength and positive current flow will give rise to a stretched wavelength. This is clearly observed in the line profiles in Extended Data Fig. 3d, f, which are obtained from averaging the 30 consecutive line scans shown in Extended Data Fig. 3c, e. For the plasmons on the right side of the gold nanobar, the wavelength difference is determined to be about 1.5% for a current of ±0.4 mA and about 3.1% for a current of ±1.2 mA. The plasmon quality for a driving current of 1.9 mA (not shown) is too low for the right side to reliably determine the plasmon wavelength shift. Our experimental observations can be captured well by the theory, as shown in Extended Data Fig. 4.

Breakdown of device at very high positive backgate voltage in thick-oxide devices

For the 2-μm SiO_2 dielectric devices, we found that the ultrahigh backgate voltage at the positive side (a few hundred volts to about 1 kV) can trigger a series of gas ionization in high vacuum where the mean free paths of the residue gas molecules become several metres. This process breaks the graphene device, as shown in Extended Data Fig. 5, and therefore we limit our measurements of the graphene plasmon at the hole doping side by applying negative backgate voltages. As the graphene holds particle–hole symmetry, the Doppler effect should be the same for the electron side[24,30].

Formation of graphene/hBN moiré superlattice in the device

The small resistance peak in our device as shown in Fig. 1c is most likely due to the formation of a graphene/hBN moiré superlattice. It has been well established in transport studies of hBN-encapsulated graphene that a second small resistance peak can be observed when the graphene and hBN align within a small angle (<2°)[46]. This alignment can often be

inferred from the alignment of straight edges between the graphene and hBN layers. To enhance the graphene and hBN contrast on the thick SiO_2 dielectric layer, Extended Data Fig. 6 shows an optical microscope picture of our device, in which we have adjusted the contrast to observe the graphene and hBN layers. As shown in the photo, the graphene straight edge (white dashed line) nearly aligns with an edge of top hBN (yellow dashed line), which can potentially form a graphene/hBN moiré superlattice with a long period. The carrier density at the small resistance peak in our device is $n_s \approx 3.98 \times 10^{12}$ cm^{-2}, which corresponds to a moiré period of around 10.3 nm and an alignment angle of around 0.93° (refs. [46,47]).

Non-equilibrium response of the plasmons in a current-carrying graphene

The optical properties of a current-carrying graphene sheet can be calculated by using linear response theory. We follow the model in ref. [30] to calculate the non-equilibrium plasmon response. The plasmon dispersion of monolayer graphene at various carrier drift velocities can be obtained as the roots of the real part of $\varepsilon(k, \omega; 0) = 1 - \frac{2\pi e^2}{q\epsilon} \chi_{nn}^{(0)}(k, \omega; 0)$, where $\chi_{nn}^{(0)}(k, \omega; 0)$ is the response function at zero temperature. ϵ and e are the effective dielectric constant of hBN and the electron charge, respectively. In the limit $\bar{k} < \bar{\omega} \ll \mu$, the real part of the response function in equation can be expanded as

$$\frac{\mathrm{Re}\chi_{nn}^{(0)}(k, \omega; 0)}{D(\mu)} \approx \frac{W(\beta)}{2\beta} \frac{\bar{k}^2}{\bar{\omega}^2} - \frac{\bar{k}^2}{8} + \gamma \frac{W(\beta)^2}{4\beta} \frac{\bar{k}^3}{\bar{\omega}^3} + \gamma \frac{\beta}{32} \frac{\bar{k}^3}{\bar{\omega}} + \frac{\bar{k}^4}{8\bar{\omega}} + \frac{3W(\beta)^2}{8\beta^2} \frac{\bar{k}^4}{\bar{\omega}^4} + \cdots,$$

$$\bar{k} = \frac{\hbar v_F k}{\mu}, \quad \bar{\omega} = \frac{\hbar\omega}{\mu}, \quad W(\beta) = 2\frac{1 - \sqrt{1 - \beta^2}}{\beta}, \tag{1}$$

where $\beta = v_d/v_F$ is the normalized electron drift velocity v_d relative to Fermi velocity v_F. μ is the chemical potential of the graphene. $\gamma = +1(-1)$ denotes 'upstream' ('downstream') plasmon propagation. $D(\mu)$ is the 2D massless Dirac fermion density of states. In the long wavelength limit $\bar{k} \ll 1$, the plasmon dispersion can be further reduced to

$$\omega_{pl}(k) = \sqrt{\frac{2D_0 W(\beta)}{\varepsilon\beta}} \sqrt{k} \left[1 + \gamma \frac{\sqrt{2\beta W(\beta)}}{4} \sqrt{\frac{k}{k_{TF}}} + \frac{12 - 16\alpha_{ee}^2 - 3\beta W(\beta)}{16} \frac{k}{k_{TF}} \right], \tag{2}$$

$$\alpha_{ee} = \frac{e^2}{\varepsilon\hbar v_F}.$$

$D_0 = \frac{e^2 E_F}{\hbar^2}$ is the Drude weight of noninteracting 2D massless Dirac fermion expressed in terms of Fermi energy E_F and the reduced Planck constant $\hbar$. $k_{TF} = 4\alpha_{ee} k_F$ is the Thomas–Fermi screening wavevector at $T = 0$ K. k_F is the Fermi wavevector.

Data availability
The data that support the findings of this study are available from the corresponding author upon reasonable request.

46. Ponomarenko, L. et al. Cloning of Dirac fermions in graphene superlattices. *Nature* **497**, 594–597 (2013).
47. Yankowitz, M. et al. Emergence of superlattice Dirac points in graphene on hexagonal boron nitride. *Nat. Phys.* **8**, 382–386 (2012).

Author contributions F.W. conceived the research. W.Z. and S.Z. carried out the near-field optical measurements. W.Z., S.Z., Sheng Wang, S.Y. and F.W. performed the data analysis. W.Z., S.Z., H.L., Shaoxin Wang, M.I.B.U, S.K., Y.J. and X.X. fabricated the graphene devices. K.W. and T.T. grew the hexagonal boron nitride crystals. All authors discussed the results and wrote the manuscript.
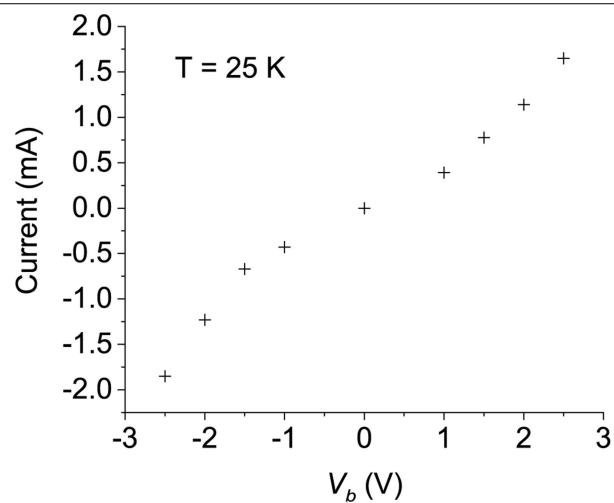
Extended Data Fig. 1 | Graphene channel current at discrete bias voltages in the two-terminal device. Measurements taken at 25 K at a carrier density of 7.0×10^{12} cm^{-2}.
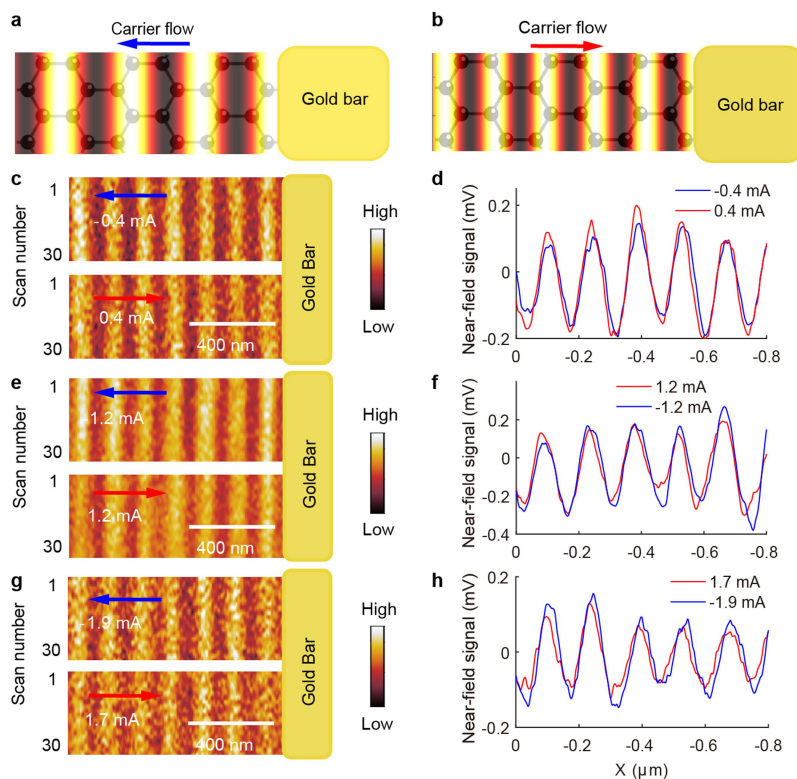
Extended Data Fig. 2 | Near-field signal of the propagating plasmon on the left side of the gold nanobar. a, b, Illustration of plasmon propagation under negative (**a**) and positive (**b**) current flows. **c, e, g,** Near-field data at −0.4 mA and + 0.4 mA (**c**), −1.2 mA and +1.2 mA (**e**) and −1.9 mA and +1.7 mA (**g**). **d, f, h,** The corresponding line profiles for **c, e, g,** respectively, averaged over the 30 scans. The gold nanobar is located on the right and the graphene plasmons propagate from the right to the left.
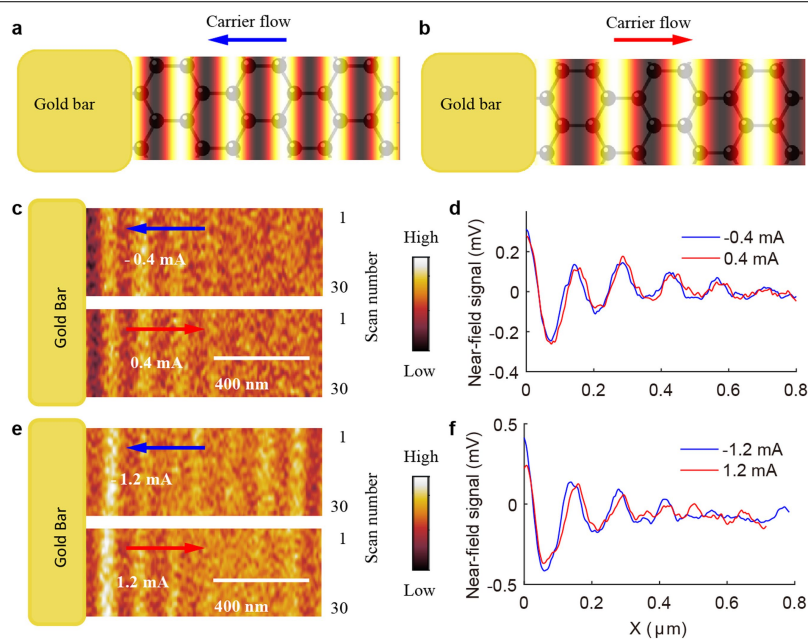
Extended Data Fig. 3 | Near-field signal of the propagating plasmon on the right side of the gold nanobar. a, b, Illustration of plasmon propagation under negative (**a**) and positive (**b**) current flows. **c, e,** Near-field data at −0.4 mA and +0.4 mA (**c**) and −1.2 mA and +1.2 mA (**e**). **d, f,** The corresponding line profiles **c, e,** respectively, averaged over the 30 scans. The gold nanobar is located on the left and the graphene plasmons propagate from the left to the right.
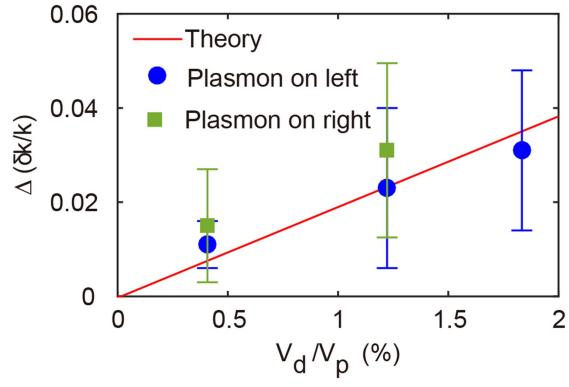
Extended Data Fig. 4 | Comparison of the Doppler effect between theory and experiment at different carrier drift velocities in the second device. The width of the graphene channel is $w = 2.5\,\mu m$ and the carrier density is estimated to be $|n| = 7.0 \times 10^{12}\,cm^{-2}$.
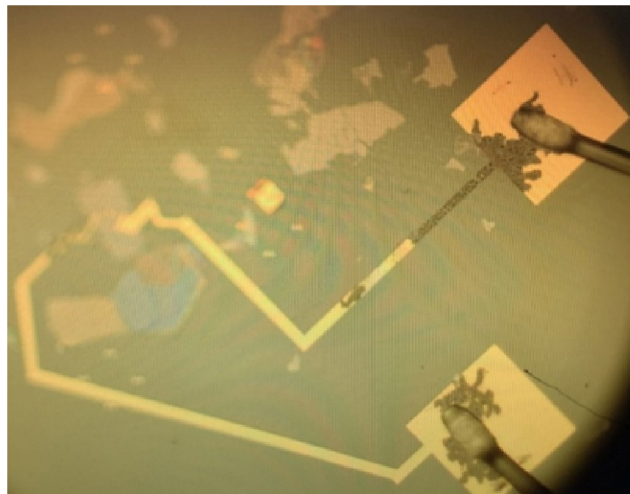
Extended Data Fig. 5 | Breakdown of device under high positive backgate voltages. The ultrahigh backgate voltage at the positive side triggers a series of gas ionization in high vacuum and damages the sample.
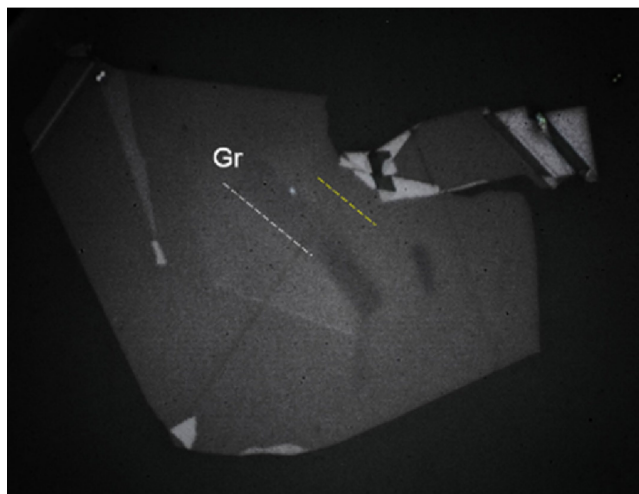
Extended Data Fig. 6 | Filtered optical image to enhance the contrast between hBN and graphene. The alignment angle between the hBN and graphene is around 0.93° and corresponds to a moiré period of around 10.3 nm, which is calculated from the carrier density ($n_s \approx 3.98 \times 10^{12} \, \mathrm{cm}^{-2}$) at the small resistance peak in our device. The white line indicates the straight graphene edge and the yellow line shows the top hBN edge.